Integrated Expression Profiling of BCR-ABL and Computational Identification of ABL1 Inhibitors in Pediatric Acute Lymphoblastic Leukemia

Shahid Ullah[1], Alex Tonks[2], Carlos Eliel Maya-Ramírez[2], Abdulsalam M Alruwaili[3], Sabahat Abdullah[4], Muhammad Arif Lodhi [1]*

1. Department of Biochemistry Abdul Wali Khan University, Mardan, Pakistan. Email: (S U) Shahidullah.phd51@gmail.com
2. Department of Hematology, Division of Cancer and Genetics, Cardiff University, School of Medicine, Cardiff, UK
3. Laboratorio de Química Supramolecular y Nanociencias, Unidad Profesional Interdisciplinaria de Biotecnología, Instituto Politécnico Nacional, Ciudad de México, México, elielmayaramirez@gmail.com
4. Northern Border University, Medical Laboratory Technology Department, College of Applied Medical Sciences, Arar, Saudi Arabia Email (AMA) Abdulsalam.Alruwaili@nbu.edu.sa
5. Shantou University Medical College, China, Email sabahatabdullah41@gmail.com

*Corresponding Author: Muhammad Arif Lodhi
Department of Biochemistry Abdul Wali Khan University, Mardan, Pakistan.
Email: arif.lodhi@awkum.edu.pk

Abstract

Pediatric B-cell acute lymphoblastic leukemia achieves overall survival approaching 90% with modern therapy, though high-risk subtypes, relapse, and drug resistance remain critical clinical challenges. Among its genetic abnormalities, the BCR-ABL fusion oncogene, resulting from the Philadelphia chromosome translocation t (9; 22), is associated with aggressive disease progression, poor prognosis, and high relapse rates, particularly in pediatric patients. This study aimed to investigate the expression profile of BCR-ABL in pediatric ALL and to identify potential inhibitors targeting the ABL1 tyrosine kinase using computational approaches. A cohort of 50 pediatric ALL patients was analysed and fusion oncogene expression was quantified using quantitative real-time PCR (qRT-PCR). BCR-ABL exhibited heterogeneous expression with several samples showing marked upregulation. To explore novel therapeutic options, a virtual screening workflow was employed using drug-like compounds from publicly available databases. Molecular docking identified four lead compounds (LIG1–LIG4) with higher binding

affinities toward ABL1 compared to the reference inhibitor imatinib. These interactions were further characterised by favourable hydrogen bonding and hydrophobic interactions within the active site. Molecular dynamics simulations over 100 ns demonstrated the structural stability of the protein–ligand complexes, supported by acceptable RMSD and RMSF profiles. Additionally, in silico ADMET and pharmacokinetic analyses indicated that the selected compounds possess favourable drug-like properties, including high gastrointestinal absorption and acceptable safety profiles. In conclusion, this study identified BCR-ABL as the most highly expressed fusion oncogene in this cohort, consistent with its known oncogenic role in Philadelphia chromosome-positive paediatric ALL, and identifies promising ABL1 inhibitor candidates through computational screening. These findings provide a foundation for further experimental validation and the development of targeted therapies for BCR-ABL–positive ALL.

Key Words: BCR-ABL, Acute lymphocytic leukaemia, Molecular dynamic simulation.

Introduction

A fusion oncogene is a genetic alteration that occurs when two different genes in a cell merge, forming a single hybrid gene that can drive uncontrolled cell growth and thus lead to cancer. The resulting fusion gene is most often created due to a chromosomal rearrangement, such as a translocation, inversion, or deletion. In this case, various parts of two previously separated genes come together. When these two genes merge, the resulting fusion protein, and therefore its activity, can be abnormal or enhanced. This disrupts normal signalling pathways in cells, leading to increased cell division and survival. As a result, these factors lead to uncontrolled cell proliferation, which contributes to the development of tumours. Fusion oncogenes have been found in various types of cancer, including leukaemia, lymphomas and solid tumours in lung and prostate cancer **[1].**

Fusion oncogenes can be detected through genetic testing and may be used to help diagnose and guide treatment for certain types of cancer. Additionally, drugs that target specific fusion proteins are being developed and tested as a precision therapy approach for some types of cancer. Acute lymphoblastic leukemia (ALL) is the most common childhood hematological cancer. While overall outcomes have improved dramatically, Philadelphia chromosome-positive (Ph+)

ALL—driven by the constitutively active BCR-ABL1 fusion oncogene—remains a high-risk subtype associated with inferior outcomes, relapse, and drug resistance despite targeted therapy with first-generation tyrosine kinase inhibitor imatinib and newer agents**[2].** The BCR-ABL1 fusion arises from the t(9;22)(q34;q11) translocation, producing a dysregulated kinase that drives uncontrolled proliferation, survival, and leukemogenesis. Current therapies have limitations: acquired resistance mutations, variable tolerability, and incomplete molecular remission in some patients. There is a clear unmet clinical need to identify novel, potent, and stable ABL1-targeted inhibitor candidates to complement or improve existing treatment options **[3].**

The prognosis for adults with ALL is dismal, with 5-year survival rates of 40% overall and around 7% for individuals who experience recurrence, despite notable advances in the treatment results for children with ALL **[4][5].**

Modern treatment protocols integrate targeted therapies and immunotherapies such as blinatumomab for high-risk ALL, with hematopoietic cell transplantation reserved for selected refractory or relapsed cases, consistent with recent COG trial findings **[6].**

It is well known that aberrant and proliferative expression of the oncogene BCR-ABL in the bone marrow cells is the prime cause of chronic myeloid leukaemia. The tyrosine kinase domain of the BCR-ABL protein has been identified as a key therapeutic target in ALL. Imatinib was the first-generation drug that could inhibit enzymatic action by stopping the BCR-ABL protein from binding to ATP. Further, the insensitivity of ALL cells was observed due to Imatinib therapy, which is a possible reason for mutation in the ATP-binding tyrosine kinase domain of the ABL receptor. Hence, some of the second-generation drugs were also reported, such as Bosutinib, Nilotinib, Dasatinib, and bosutinib, etc which can act against the mutated domain of the ABL tyrosine kinase protein. Nonetheless, considering issues of bioavailability and acquired resistance, there is a need for more inhibitors for the mutated ABL tyrosine kinase protein. For virtual screening, a dataset was created which includes all available drug-like natural compounds collected from ZINC and Drug Bank databases. The comparative docking analysis was also done for the active site of ABL tyrosine kinase receptor with the reported reference inhibitors.

In this study, we quantified BCR-ABL expression across 50 pediatric ALL samples and observed marked heterogeneous upregulation, supporting its clinical relevance as a key oncogenic driver

in Ph+ ALL. This finding directly motivated our subsequent computational screening to identify novel, potent ABL1-targeted inhibitor candidates

Given the critical role of BCR-ABL in leukemogenesis, this study not only evaluates its expression profile in pediatric ALL patients but also explores potential therapeutic inhibitors through computational screening targeting the ABL1 kinase domain.

Material and Methods

Ethical Approval

The study was approved by the Institutional Review Board (IRB) of Abdul Wali Khan University, Mardan, Pakistan (Approval No. Dir A&R AWKUM 2020/5118). Written informed consent was obtained from all participants or their guardians in accordance with ethical guidelines.

Study Population and Sample Collection

A total of 50 children and adolescents diagnosed with acute lymphoblastic leukaemia (ALL) patients (29 males and 21 females) aged between 2 and 20 years were included in the study. Control samples for expression comparison were defined as Philadelphia chromosome-negative (Ph−) pediatric ALL patients. Patients who received imatinib or other ABL-directed tyrosine kinase inhibitors (TKIs) prior to sample collection were excluded from this study to avoid confounding effects of TKI exposure on BCR-ABL expression levels. Samples were collected at early diagnosis before starting standard chemotherapy where possible. Complete Philadelphia chromosome status and BCR-ABL transcript subtype data were not available for this retrospective cohort. Peripheral blood samples were collected from patients undergoing treatment at oncology and haematology clinics. Approximately 4 mL of venous blood was collected in EDTA tubes using standard venipuncture procedures. Patients diagnosed with acute myeloid leukaemia or severe systemic illnesses were excluded. Clinical and demographic data were obtained from hospital records.

Hematological Analysis

Complete blood counts (CBC) were performed using an automated haematology analyser **(**Sysmex XT-4000i, Sysmex Corporation, Japan**).** Peripheral blood smears were prepared and stained using May-Grünwald and Giemsa staining**.** Slides were examined under a microscope by an experienced haematologist to assess blast cell morphology and confirm leukaemia phenotype.

RNA Extraction and cDNA Synthesis

Total RNA was extracted from peripheral blood samples using the GeneJET RNA Blood Mini Kit (Thermo Fisher Scientific) according to the manufacturer's instructions. RNA samples were treated with RNase-free DNase I to remove genomic DNA contamination. First-strand cDNA was synthesised using the RevertAid First Strand cDNA Synthesis Kit (Thermo Fisher Scientific) following the manufacturer's protocol.

Real-Time PCR

Gene expression analysis was performed using SYBR Green-based quantitative real-time PCR (qRT-PCR) on an Applied Biosystems StepOne™ Real-Time PCR System. The ABL gene was selected as the endogenous reference gene based on validated evidence from recent studies (PMID: 35344115, 37156894, 34783280), which confirm ABL exhibits minimal expression variability and superior stability compared to other commonly used housekeeping genes in leukemia and acute lymphoblastic leukemia samples.

Primers used were adopted from established standard protocols (Van Dongen et al., 1999). BCR-ABL primers target the unique BCR–ABL fusion junction region, while ABL reference primers amplify a distinct native ABL gene segment—this sequence-specific design prevents cross-hybridization and eliminates non-specific co-amplification of native ABL in BCR-ABL assays. Full primer details, positions, sequences, and amplicon information are listed below:

For BCR-ABL fusion transcript:

Forward (BCR F): Position 402 — CACTCAGACCCTGAGGCTCAA
Reverse (ABL R): Position 561 — CTGGCCCAACGATGGCGA
Target/amplicon coordinates: 1727–1744 (18 bp); 277–257 (21 bp)
For reference ABL gene:

Forward (ABL F): Position 1003 — GATGTAGTTGCTTGGGACCCA
Reverse (ABL R): Position 1063 — TGGAGATAACACTCTAAGCATAACTAAAGGT

Amplicon sizes: 372 bp (31 bp); 495 bp (21 bp)

Each reaction was carried out in a total volume of 25 µL containing 12.5 µL of SYBR Green/ROX Master Mix (2×), 0.3 µM of each forward and reverse primer, up to 500 ng of cDNA template, and nuclease-free water to complete the volume. Thermal cycling conditions were: initial denaturation at 95°C for 10 minutes, followed by 40 cycles of denaturation at 95°C for 15 seconds and combined annealing/extension at 60°C for 60 seconds. Amplification efficiency was validated using 5-fold serial dilution standard curves, consistently falling within the acceptable range of 90–110%. Melting curve analysis confirmed single, specific amplification products for all assays. ABL showed highly consistent threshold cycle (Ct) values with low variation across all patient samples, confirming its stability and reliability as a single reference gene. All reactions were performed in duplicate or triplicate to ensure reproducibility; no-template controls were included in every run to detect potential contamination **[7]**.

Relative Gene Expression Analysis

BCR-ABL showed substantial heterogeneous expression across samples, with a wide range of fold change values (0.04–92.41) and several samples exhibiting marked up regulation. Notably, complete Philadelphia chromosome status and transcript subtype data were not available for this retrospective cohort; this broad expression range likely reflects a mixed patient population, consistent with the known high oncogenic expression of BCR-ABL in Philadelphia chromosome-positive ALL cases.

Relative gene expression was quantified using the 2^-ΔΔCt method (Livak and Schmittgen, 2001). The threshold cycle (Ct) values were used to calculate ΔCt as follows:

ΔCt = Ct (target gene) − Ct (housekeeping gene)

ΔΔCt was calculated by normalizing each sample to the mean ΔCt of the control group:

ΔΔCt = ΔCt (sample) − mean ΔCt (control)

Fold change was determined using:

Fold change = 2^(-ΔΔCt)

All samples were analysed in duplicate, and average Ct values were used for calculations. The mean ΔCt of control samples (1.28) was used as the calibrator.Extreme values (fold change >100) were assessed during analysis; however, no such values were present in the final dataset **[8].**

Molecular docking

The active site residues of the ABL1 protein were confirmed using an extensive literature study **[9]** and validated using the Site Finder tool of the Molecular Operating Environment (MOE). Drug like compounds were retrieved from the ZINC database (doi.org/10.1021/acs.jcim.2c01253) to perform a virtual screening encompassing approximately 5,000 molecules. Prior to docking protein preparation, ligand optimization, were carried out using the MOE software. The selected compounds were ranked based on docking S-score, predicted binding energies, and interactions pattern with key residues within the ABL1 active pocket. The highest ranked compounds were subsequently selected for molecular dynamics simulations and pharmacokinetic evaluation. Through the triangle algorithm, the optimal poses between docked molecules were discovered; however, the London DG function presented comprehensive information within re-scored simulated poses **[11].** Ten poses were created and reduced by force fields. As receptor residues were made rigid, binding energies were calculated using a combination of generalized born solvation models **[12].** The top three compounds from the docking study based on binding energy, S-score function, and RMSD were further explored.

Examination of Ligand-Receptor Interaction

The ligand-receptor interactions analysis was done using MoE's ligX tool, which gave the 2D receptor plots for both docked complexes **[14].** The ligand interaction investigations largely focused on hydrogen bonding, electrostatic, non-electrostatic, and hydrophobic interactions, thereby confirming the hydroxyl group's interaction through hydrogen bonding and the binding of chemicals at the protein's active site concurrently. Secondly, the 3D structure visualisation of complex molecules was done using PyMOL software **[15].** Molecular dynamics simulations were done using the top four chemicals from the docking study, which were considered hits.

Molecular Dynamics Simulation

MD simulations were performed using Desmond with the OPLS 2005 force field and the TIP3P water model, utilised to simulate the protein, as previously reported [16]. Similarly, a TIP3P water box with orthorhombic size dimensions 10 Å × 10 Å × 10 Å was used and neutralised with 0.15 NaCl **[16]**. Equilibration involved a restrained minimisation strategy to gradually relax the system while preserving protein coordinates. Relaxation of the system was achieved using steepest descent and Limited-memory Broyden-Fletcher-Goldfarb-Shanno (LBFGS) algorithms

[17]. Subsequently, simulations spanning 5 ns were performed under the NPT ensemble utilizing Berendsen thermostat and barostat techniques to maintain temperature and pressure **[18]**. The Hoover thermostat algorithm maintained the temperature at 300 K, while the pressure was regulated at 1 atm using the Martyna-Tobias-Klein Barostat algorithm **[19,20]**. Short-range columbic interactions were addressed with a cutoff value of 9.0 Å, while long-range columbic interactions were managed using the smooth particle mesh Ewald technique and SHAKE algorithm **[21, 22]**. Covalent and hydrogen bond atoms were constrained within a tolerance of 109 Å **[23]**. This equilibration phase served solely for system relaxation and was not included in subsequent trajectory analyses. After completion of the equilibration stage, unrestrained production MD simulations were performed for 100 ns with trajectory sampling every 1.2 ps, resulting in a total of 1000 frames, and all structural analyses, including RMSD, RMSF, PCA, SASA, and intermolecular interaction analyses, were derived exclusively from the production trajectories **[24, 25]**.

Post MD simulation Analysis

This study examines MD trajectories obtained through simulations conducted using the Maestro graphical interface (Schrodinger 2016-4) **[26]**. The RMSD and RMSF of complexes were computed with respect to the initial structure as a reference. Throughout the simulation, interactions and contacts between complexes (receptors and ligands) were assessed **[27]**. The methodology utilised molecular mechanics potential energy (Van der Waals, Electrostatics) and free solvation energy to determine the overall energies of the system, utilising snapshots from a 100 ns MD simulation **[28]**. Grant et al. (2021) employed the Bio3d package in R Studio to analyse protein dynamics based on MD trajectories, utilising principal component analysis (PCA) **[29]**. PCA is a commonly utilised technique for scrutinising protein structure and dynamics from MD trajectories. It suggests that frame-by-frame conformational fluctuations can be interpreted as a linear combination of the essential dynamics extracted through PCA **[30]**.

Results and Discussion

Clinical characteristics of the selected ALL patients

A total of 50 pediatric ALL patients were included in the study, comprising 29 males and 21 females, with a median age of 7 years. Hematological analysis showed marked abnormalities in several blood parameters. The mean total leukocyte count was 89,767/cmm, while the mean platelet count was 104,238/cmm and the mean hemoglobin level was 8.25 g/dL, indicating leukocytosis and anemia in a substantial proportion of cases. In addition, the percentage of immature cells and blast cells was elevated in most patients, reflecting the leukemic burden. These findings are consistent with the typical hematological profile of acute lymphoblastic leukemia and support the clinical classification of the included cases.

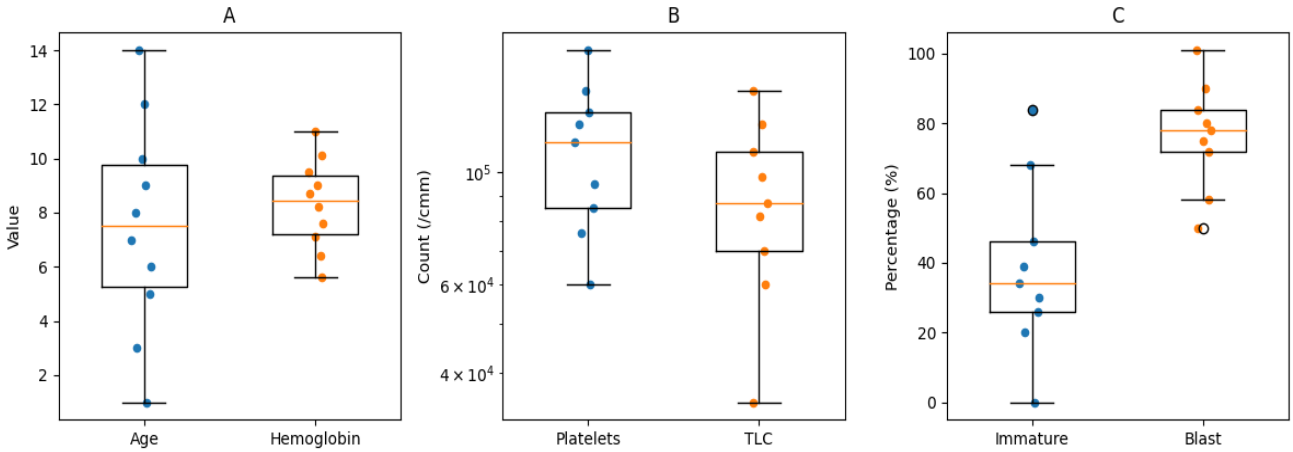

Figure 1. Clinical characteristics of paediatric acute lymphoblastic leukaemia patients. (A) Distribution of age and hemoglobin levels. (B) Platelet count and total leukocyte count (TLC) shown on a logarithmic scale. (C) Percentage of immature cells and blast cells. Data are presented as box plots with overlaid individual sample points.

BCR-ABL Expression Analysis

Relative quantification of BCR-ABL expression was performed using the 2^-ΔΔCt method, with the mean ΔCt of control samples (1.28) used as the calibrator. The analysis revealed substantial inter-sample variability in gene expression levels.

The mean fold change was 18.00 ± 23.47 (mean ± standard deviation)**,** with values ranging from 0.04 to 92.41**,** indicating a wide dispersion of expression across samples. Several samples demonstrated pronounced upregulation, with fold changes exceeding 30, whereas others exhibited reduced expression levels below baseline (fold change <1.0).

Notably, complete Philadelphia chromosome status was not available for this retrospective cohort. The broad expression range observed (0.04–92.41 fold change) most likely reflects a mixed patient population: comprising Ph+ cases with high oncogenic BCR-ABL expression alongside Ph− cases with low-level or background transcript signals.

The distribution of expression values was positively skewed, characterized by a subset of high-expression cases alongside a majority of samples with moderate or low expression levels. This pattern reflects the heterogeneous nature of BCR-ABL expression among leukaemia patients and suggests variability in oncogenic activation across different cases. Importantly, no samples exceeded the predefined exclusion threshold of 100-fold change, supporting the robustness and reliability of the dataset. These findings are consistent with the biological heterogeneity commonly observed in BCR-ABL–positive leukaemia.

Based on the observed variability in expression, subsequent computational analyses were conducted to identify potential inhibitors targeting the ABL1 kinase domain.

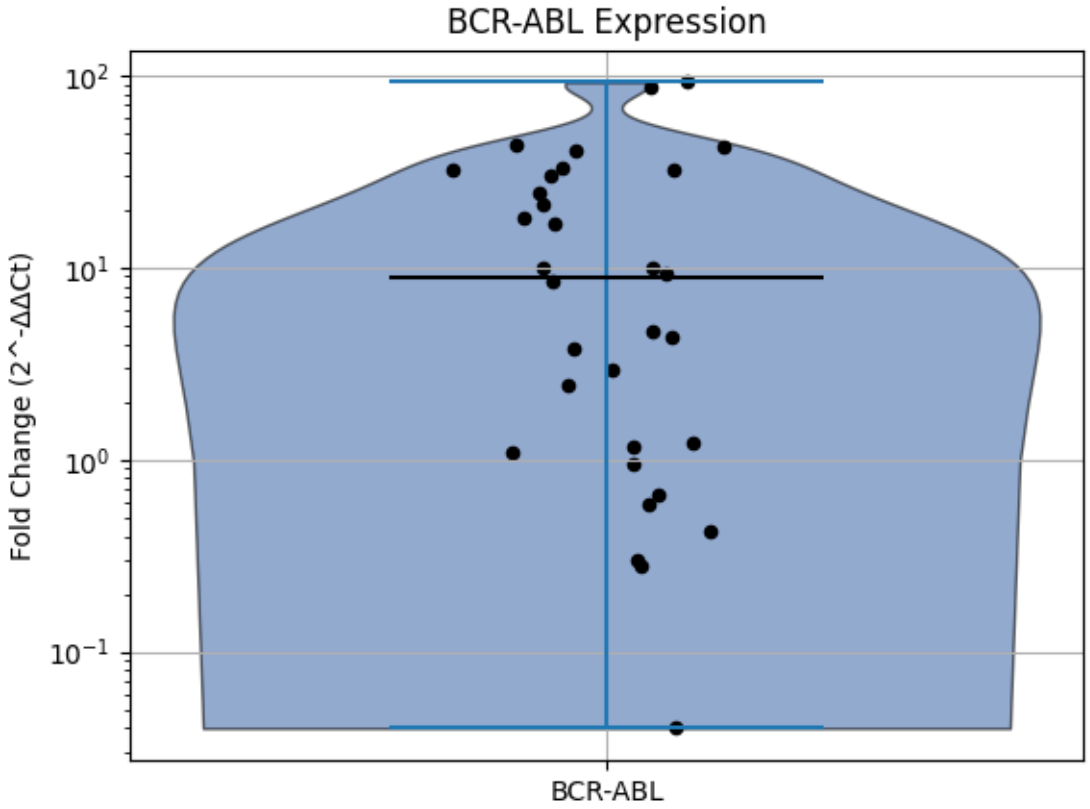

Figure 2. Violin plot representing the distribution of BCR-ABL expression levels (2^-ΔΔCt, log scale) across samples. The width of the violin indicates data density, while individual data points are overlaid to illustrate inter-sample variability. The distribution shows a positively skewed pattern with several high-expression cases.

Control docking and Virtual Screening

Many research projects are being conducted to discover new molecular entities and solve the difficult problem of drug resistance **[31]**. Drug-resistant ABL1 tyrosine kinase variations have become a major healthcare concern in recent years. While tyrosine kinase inhibitors (TKIs) of the second and third generations have demonstrated enhanced effectiveness against resistant strains, long-term survival rates have not been appreciably affected by them **[32]**. The investigation of novel compounds originating from organic small molecule inhibitors and natural sources is promising for the advancement of clinical treatments in the future **[33]**. Computational techniques, used together in biological and experimental research, may assist researchers in

learning more about drug resistance mechanisms and speed up the hunt for new molecule inhibitors **[34]**. To acquire insight into the atomistic scale binding mechanism between ABL1 and inhibitors, the molecular docking technique was used. The docking compounds were selected based on four main criteria: the optimal interaction pattern in the active pocket with minimum Gibbs free energy, hydrogen bond propensities, and potential non-covalent interactions with the highest estimated s-score function. The top-ranked poses were selected amongst 5000 docked compounds. The criteria for ranking included thresholds that required a ligand to show the required S-score values (the lower S-score, the better binding affinities, and interactions) in association with the ABL1 target that included all the binding hotspot residues. Furthermore, the compounds library retrieved from the zinc database was docked inside the defined binding pocket of ABL1, while the co-crystallized ligand imatinib was used and treated as a control for ABL1 to determine the exact conformational pose. As observed in the experimental crystal structure of ABL1 (PDB: 6HD6) several key residues were observed to establish bonds with the core residues of ABL1. Specifically, the amino residues E305, T334, M337, I379, and D400 were the key residues involved in the formation of hydrogen bonds with the amide and carboxylic groups of imatinib. The docked complex showed an RMSD of 0.014 Å against the control solved crystal complex. In the control docking analysis, the focus shifted to the exact confirmation, where the residue T334 was found to facilitate hydrogen bond interaction with the carboxylic group of imatinib exhibiting the docking s-score -10.9130 kcal/mol. Moreover, in virtual screening, the docking complexes were evaluated based on the binding s-score and interaction pattern of the inhibitors bound in the active site of ABL1. Table 1 shows the four most promising inhibitors for ABL1 ranked on binding S-score from top to bottom. LIG1 exhibited the most favorable S-score among the screened molecules, indicating a higher predicted binding potential within the ABL1 active pocket compare to the reference ligand. LIG1 exhibited the highest binding s-score (-16.3130 kcal/mol) usually ranked on the top of the list followed by LIG2, LIG3, and LIG4 (-15.9112 kcal/mol, -14.0093 kcal/mol, and -13.6895 kcal/mol) having significantly lower binding energies in comparison with LIG1. The hydrogen bonds, hydrophobic interactions, and the binding mechanisms of inhibitors bonded with ABL1 play a vital role in stabilising protein-ligand complexes and increasing binding energies.

Table 1. The top hit binders with their zinc ID were screened by MOE along with their S-score

Compounds	S-score	Hydrogen Bonds	Vdw and hydrophobic Interactions
Imatinib	-10.9130	T334	GLU305, ASN342, ASP400, THR334
ZINC98605055 (LIG1)	-16.3130	E305, D400	K209, M309, L317, L373, R381, D382, H380, A399, F401
ZINC98603938 (LIG2)	-15.9112	K290, E298, E305, D400	E301, F302, E305, G402, L406
ZINC98605017 (LIG3)	-14.0093	E301, E305, D400	E298, K304, M309, E311, G402
ZINC98604470 (LIG4)	-13.6895	K290, E305, D400	E298, E301, F302, V308, M309

Interactions reported are persistent contacts observed during 100 ns molecular dynamics simulation.

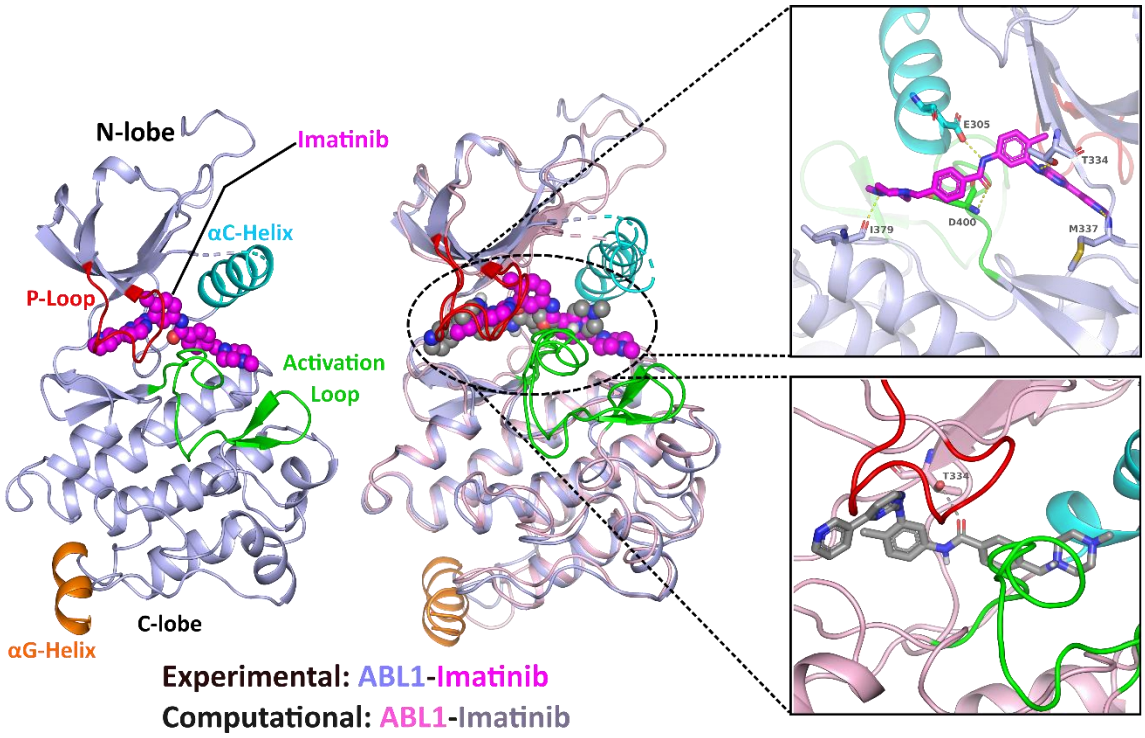

Figure 3. Redocking of the ABL1 with **co-crystalised compound imatinib in the binding pocket of the ABL1** to identify the exact conformational pose. In both panels, the crystal structure ABL is bound with imatinib in blue and magenta, while the redocking complex is represented as pink and grey.

Binding interactions of Hit molecules with ABL1

The ZINC98605055 (LIG1) exhibiting the highest binding s-score -16.3130 kcal/mol, bound within the binding pocket of ABL1, observed with two hydrogen bonds formed via interactions with the hydroxyl group of E305 and D400 residues, with their bond lengths 2.2 Å, respectively.

Apart from hydrogen bonds, K209, M309, L317, L373, R381, D382, H380, A399, and F401 were the key residues observed in VDW and hydrophobic interactions. Furthermore, the ZINC98603938 (LIG2) bound with ABL1 exhibits a slightly lower binding s-score -15.9112 kcal/mol observed with four hydrogen bonds engaged by carboxylic and amide groups of the residues K290, E298, E305, and D400 with distances measured between 2.2 Å-3.0 Å, respectively. Other residues that encounter strong van der Waals interactions included E301, F302, E305, G402, and L406. Additionally, ZINC98605017 (LIG3) showed a lower binding s-score (-14.0093 kcal/mol) compared with LIG1 and LIG2, observed with three hydrogen bonds formed via interactions with the carboxylic and hydroxyl groups encapsulated by the residues E301, E305 and D400 near the amide group of LIG3 at distances measured 1.9 Å, 2.5 Å, and 2.7 Å, respectively. Moreover, the residues E298, K304, M309, E311, and G402 were also observed as strong coordination in VDW and hydrophobic interactions inside the active pocket, which play a vital role in the ligand stability. Moreover, the basic interaction skeleton for the ZINC98604470 (LIG4) bound with ABL1 made a possible interaction through energy contribution of -13.6895 kcal/mol, examines three hydrogen bonds by key player residues K290, E305 and D400 near the amide and hydroxyl moieties of LIG4 with their bond lengths 2.2 Å, 2.3 Å and 2.7 Å, respectively. As opposed to these hydrogen bonds, VDW and hydrophobic interactions engaged by the residues E298, E301, F302, V308 and M309 as shown in **Fig 4**.

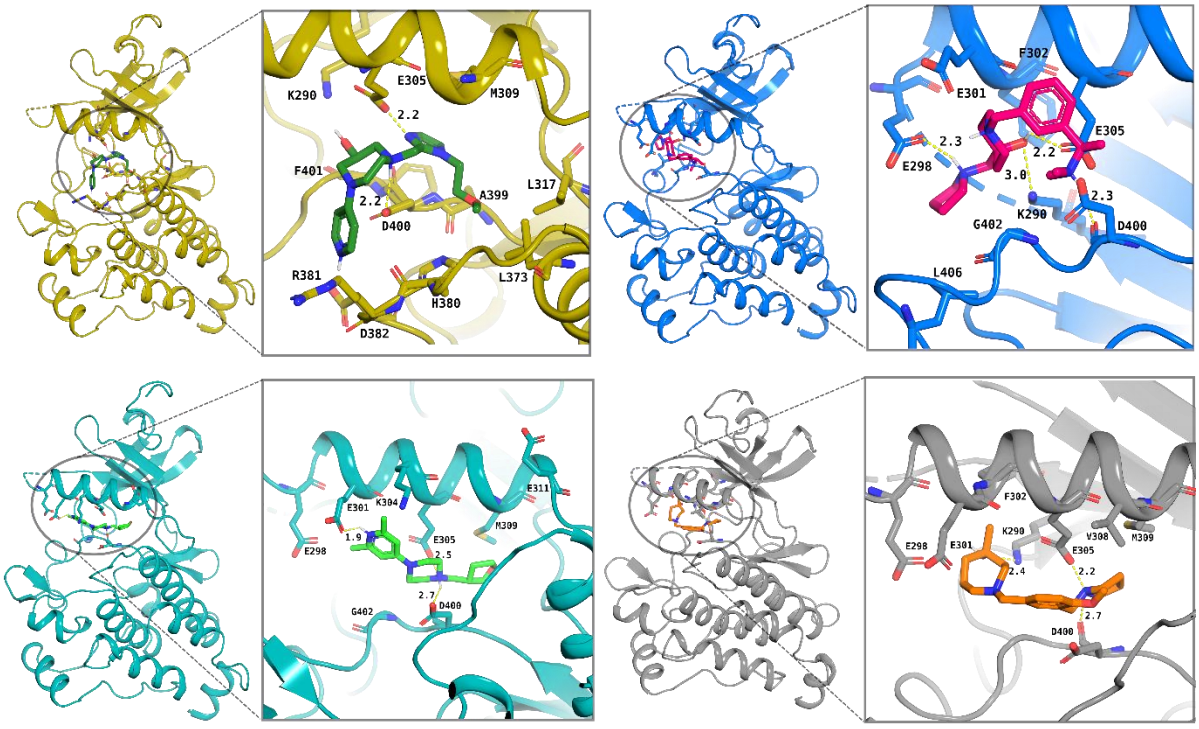

Figure 4. The binding mode of the top hit inhibitors in complex with ABL1. These hit inhibitors encapsulated in the active site of the ABL1 are represented as sticks with their respective dark green, hot pink, light green, and orange colours.

MD simulation

Simulations were monitored until structural convergence was achieved, as indicated by RMSD stabilisation. Simulations were terminated once RMSD values stabilised, indicating structural equilibrium. Five ligand protein-ligand complexes were run for 100 ns to test the stability and binding mode of the identified inhibitors against the control imatinib. The co-crystalised imatinib was treated as a control, whereas the four identified hit molecules were selected based on their binding scores and interaction patterns. The MD simulation trajectories were evaluated for protein perturbations using RMSD and RMSF values to assess alterations in amplitude across 100 ns of time scales. This study examines the conformational changes caused by the interaction of four inhibitors (LIG1-LIG4), including whether they affect the complete protein structure or regions. The RMSF graph shows protein structural changes that occur before inhibitor binding. Low RMSD values indicate minimal structural changes and suggest system stability. Molecular dynamics (MD) simulations provide precise insights into the conformational landscape of protein-ligand complexes, allowing them to closely mimic physiological configurations. In this

study, MD simulations were performed on the top four ABL1-imatinib complexes, namely ABL1-LIG1, ABL1-LIG2, ABL1-LIG3, and ABL1-LIG4 utilizing the Schrodinger (v. 2020-4) Desmond module. To further elucidate the conformational stability of the docked complexes, trajectories were generated for statistical analysis of RMSD and RMSF. Calculating the average distance of a simulated protein-ligand interaction is the main application of RMSD. Consequently, from each 100 ns simulation trajectory, RMSD values for the protein (Ca) and the protein-fit ligands were determined, as shown in **Figure 5.** The ABL1 complex exhibited average fluctuations of the c-alpha atoms below 3 Å when interacting with screened compounds, which is conducive for small globular proteins. In the RMSD plot of the LIG-imatinib complex, initial spikes in RMSD deviation were observed up to 40 ns (3.4 Å), after which the complexes stabilised towards the end of the simulation. The RMSD from initial points was lower in subsequent regions, ranging from 2.2 Å. The overall RMSD range is observed between 0.8 ± 3.2 Å. The RMSF protein fluctuations peaked at residues 292–296, 244-246, 410-415, and 470-475 throughout the simulation. However, most residues exhibited a decrease in RMSF, with values ranging from 1.2 Å. Initially, the RMSD for LIG-2 rose to 2.28 Å by the 20 ns mark before the protein stabilised over the course of the 100 ns simulation. Notably, residues 244-247, 292-295, 420-425, and 542-545, as well as regions 295–298, displayed higher RMSF values ranging from 0.6 to 4.8 Å. In the docked ABL1-LIG2 complex, the Ca-atoms exhibited higher RMS deviation, averaging between 0.4 and 2.8 Å up to 30 ns, followed by a slight increase and eventual equilibrium with a mean RMS deviation of 2.8 to 1.6 Å over 100 ns, as shown in **Figure 5**. During this period, deviations were observed in the C-termini of the protein within the plot. The RMSF analysis graph showed similar trends to Ligand 1, with high fluctuations observed in the areas encompassing residues 244-247, 292-295, 420-425, and 542-545, primarily in the loop regions. Despite these fluctuations, the overall RMSF values ranged from 0.6 to 5.4 Å within the structures.

Alpha helices and beta strands typically exhibit lower levels of fluctuation compared to loop regions due to their inherent rigidity. Conversely, catalytic residues and other functional areas tend to demonstrate greater stability, with fluctuations occurring at a smaller amplitude. The ABL1-LIG3 complex displays distinct characteristics compared to the aforementioned complexes, as it exhibits no significant amplitude of deviation. Initially, fluctuations are observed from 0 to 5 ns, followed by stability, although high fluctuation is observed between 15

and 45 ns. Despite occasional stability points up to 70 ns, the overall RMSD values range between 0.6 and 2.8 Å. On the other hand, ABL1 and LIG4 demonstrate higher deviation from 0 to 25 ns, with values ranging from 0.5 to 2.25 Å. Subsequently, the complexes stabilise until the end of the simulation, with overall values ranging between 0.5 and 2.25 Å. While the RMSF graph exhibits similarities to other ligands, depicting higher fluctuation in similar regions, there are differences in the values observed.

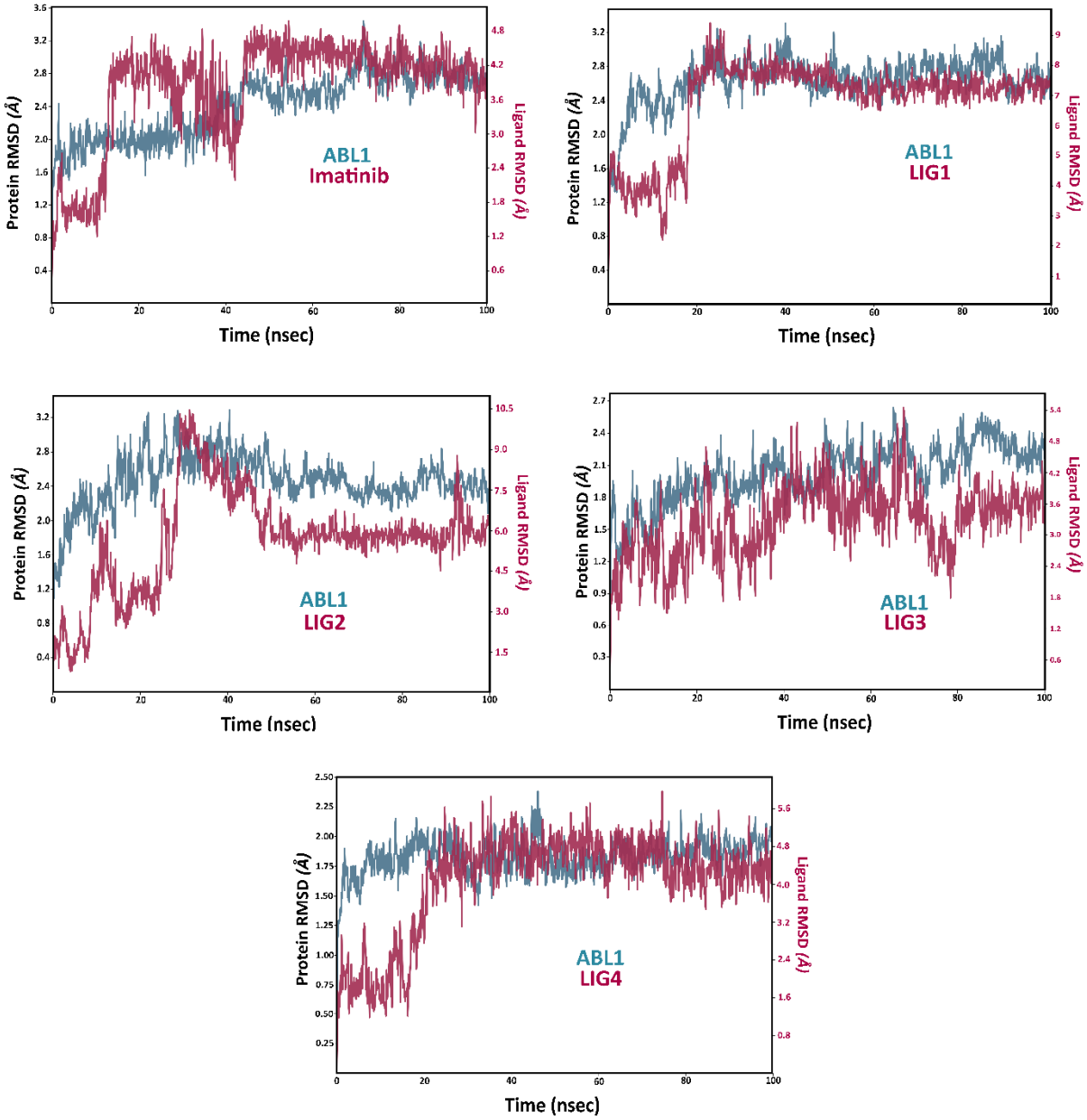

Figure 5: Root mean square deviation (RMSD) of the selected inhibitors along with the co-crystalline ligand (control) bound in the pocket of ABL1 with a timescale of 100 ns simulation system.

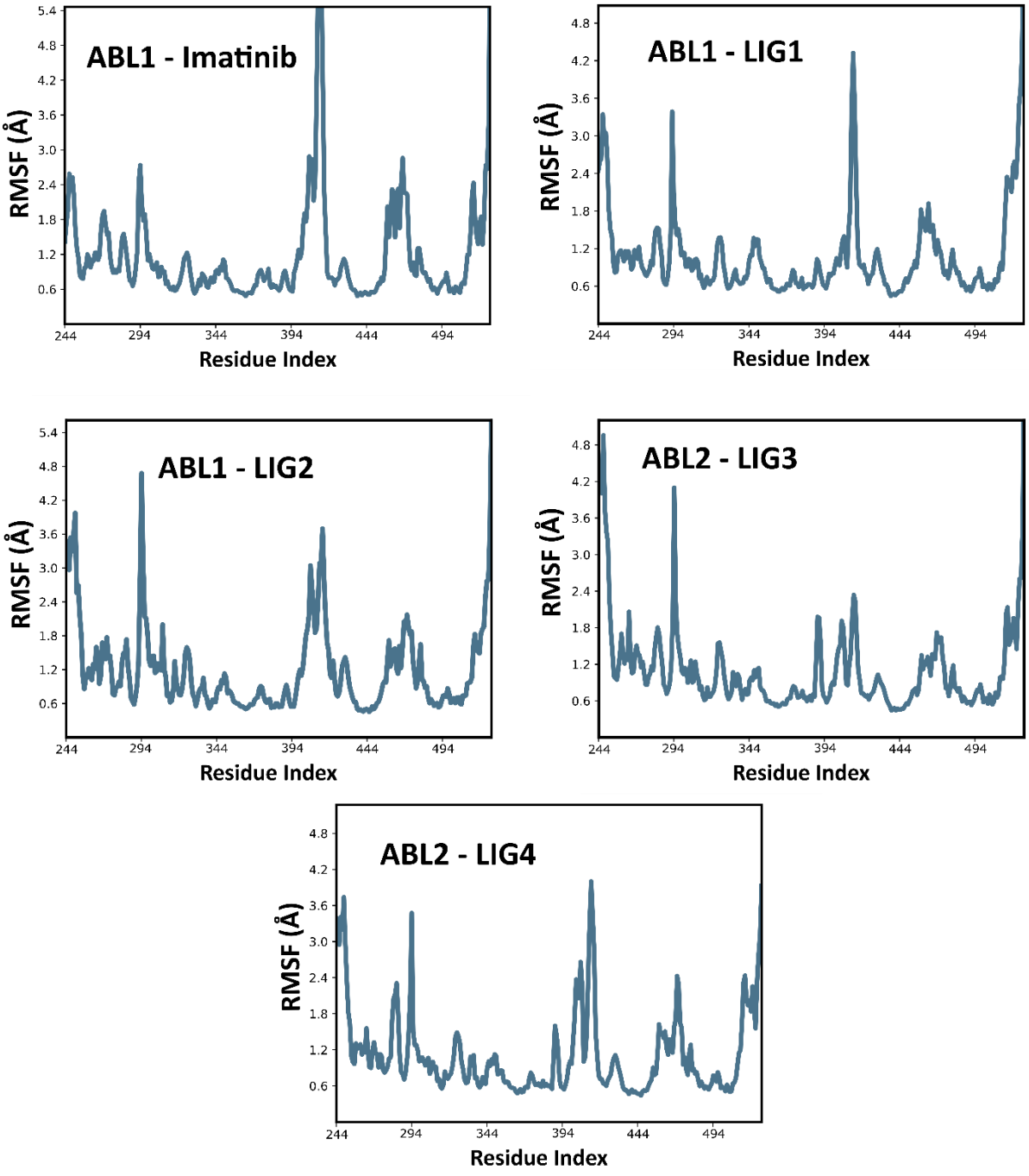

Figure 6: Root means square Fluctuation (RMSF) of the selected inhibitors along with the co-crystalline ligand (imatinib) bound in the pocket of ABL1 with a timescale of 100 ns simulation system.

Preservation of intermolecular contacts in molecular dynamics simulation

The inhibitors in the imatinib-ABL1 complex exhibit various intermolecular interactions, including hydrogen bonds, hydrophobic interactions, ionic interactions, and water bridges, as illustrated in the stacked bar chart plot. Specific subtypes of these interactions were explored through the simulation interactions diagram presented in **Figure 5**. In the ABL1-imatinib complex, several residues within the protein structure are involved in forming hydrogen bonds, hydrophobic interactions, and water bridges, as shown in **Figure 7**. For instance, residues GLU305, ASN342, ASP400, LEU267, TYR272, ALA288, PHE336, LEU389, PHE401, LEU403, MET407, THR334, GLU335, ASP344, ARG347, and ASP400 contribute to these interactions. Within the ABL1-LIG1 complex, distinct types of interactions stabilise the complex, including hydrogen bonds involving residues GLU298/301, 305, and ASP400. Additionally, hydrophobic interactions are observed with residues VAL308, ILE312, LEU373, ARG381, and 405, while water bridges are formed by residues LYS290, GLU301, LYS304, ILE397, HIS380, ASP382, ASP400, and SER404. Critical residues forming hydrogen bonds in the ABL1-LIG2 complex include GLU298/301, GLU305, and ASP400. Hydrophobic interactions involve residues VAL308, LEU317, VAL318, LEU373, PHE378, and HIS380, while water bridges are observed among residues LYS304, ILE379, and GLY402. Ionic interactions involve GLU305, SER404, and ARG40. Hydrogen bonding within the ABL1-LIG3 complex depends critically on critical residues like ASP400 and GLU301/305. In addition, residues VAL308, ILE312, PHE378, HIS380, and ARG381 are involved in hydrophobic interactions. Water bridges are also seen between residues THR291, GLU298 and PHE401 and LYS290. Hydrophobic contacts are mediated by residues VAL308, MET309, HIS380, ARG381, and ALA418 in the ABL1-LIG4 complex, whereas hydrogen bonds are generated with residues GLU301, GLU305, and ASP400. Water bridges are seen when ASP400 and GLU305 residues are present. Residues that participate in many interactions, such as hydrogen bonds, ionic bonds, and water bridges, include GLU305 and ASP400.

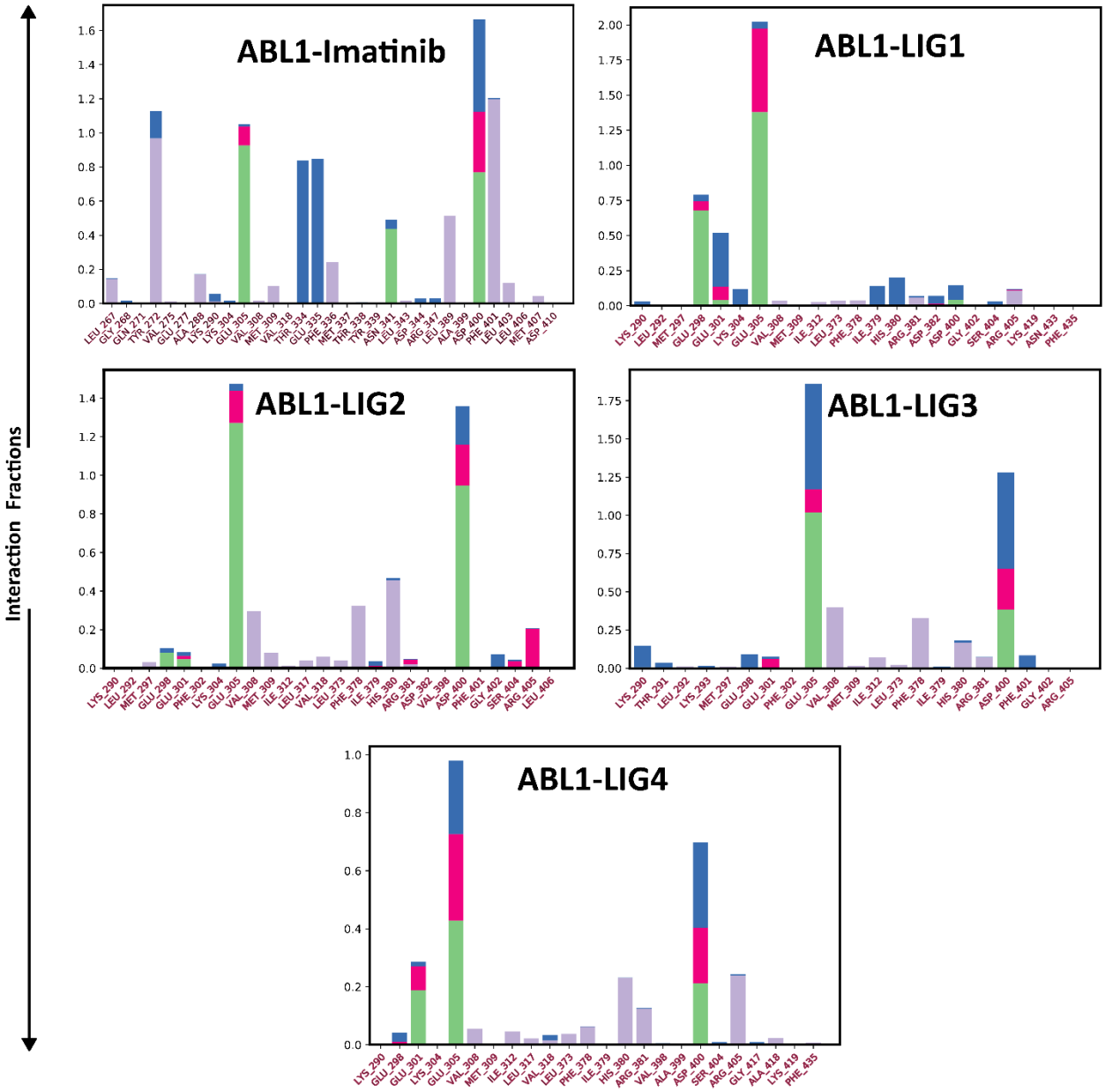

Figure 7: Various intermolecular interactions formed by binding residues with selected top inhibitors observed in the molecular dynamics simulation.

Principal Component Analysis

The primary motions within the protein structure were determined using PCA via the Bio3d package (Grant et al., 2021). This method utilises a mathematical covariance matrix to capture diverse dynamic patterns observed by the system over the explored time scale, with analysis conducted relative to an initial reference structure. PCA focused on backbone atoms to elucidate the dominant free motions of ligands. The protein's movements were categorised into 2D

patterns at different stages, such as ligand binding and retention. Furthermore, PCA analysis explored the impact of ligands on protein confirmation dynamics, revealing that all ligands bind within the active site of ABL1. The eigenvectors of the control complex (ABL1-Imatinib) and LIG1-4 accounted for 35.28%, 20.9%, 26.2%, 23.15%, and 26.78% of the total confrontational variance, respectively, indicating no significant coordinate movements during the simulation. The changes in the variance percentage explained by the first principal component reflect ligand dependent modulation of the conformational landscape of ABL1 rather than differences in structural stability. From PCA analysis, it can be inferred that LIG1-4 binding to ABL1 protein results in a stable conformational change. The comparatively higher variance observed for the LIG1 complexes indicates that a larger fraction of the collective motion was captured by the first PC1, whereas the lower values obtained for LIG2 and LIG3 suggest that the conformational fluctuations are distributed across multiple principal components. Additionally, red colours signify lower PC values, reflecting reduced docking ability. This limited mobility is consistent with the results of Rg analysis, which demonstrate that the presence of LIG1, LIG2, LIG3, and LIG4 induces a contraction in protein conformation dynamics. Protein geometries with such compactness can effectively hinder substrate interactions. The PCA plots reveal significant disparities in conformations, as shown in **Figure 8.**

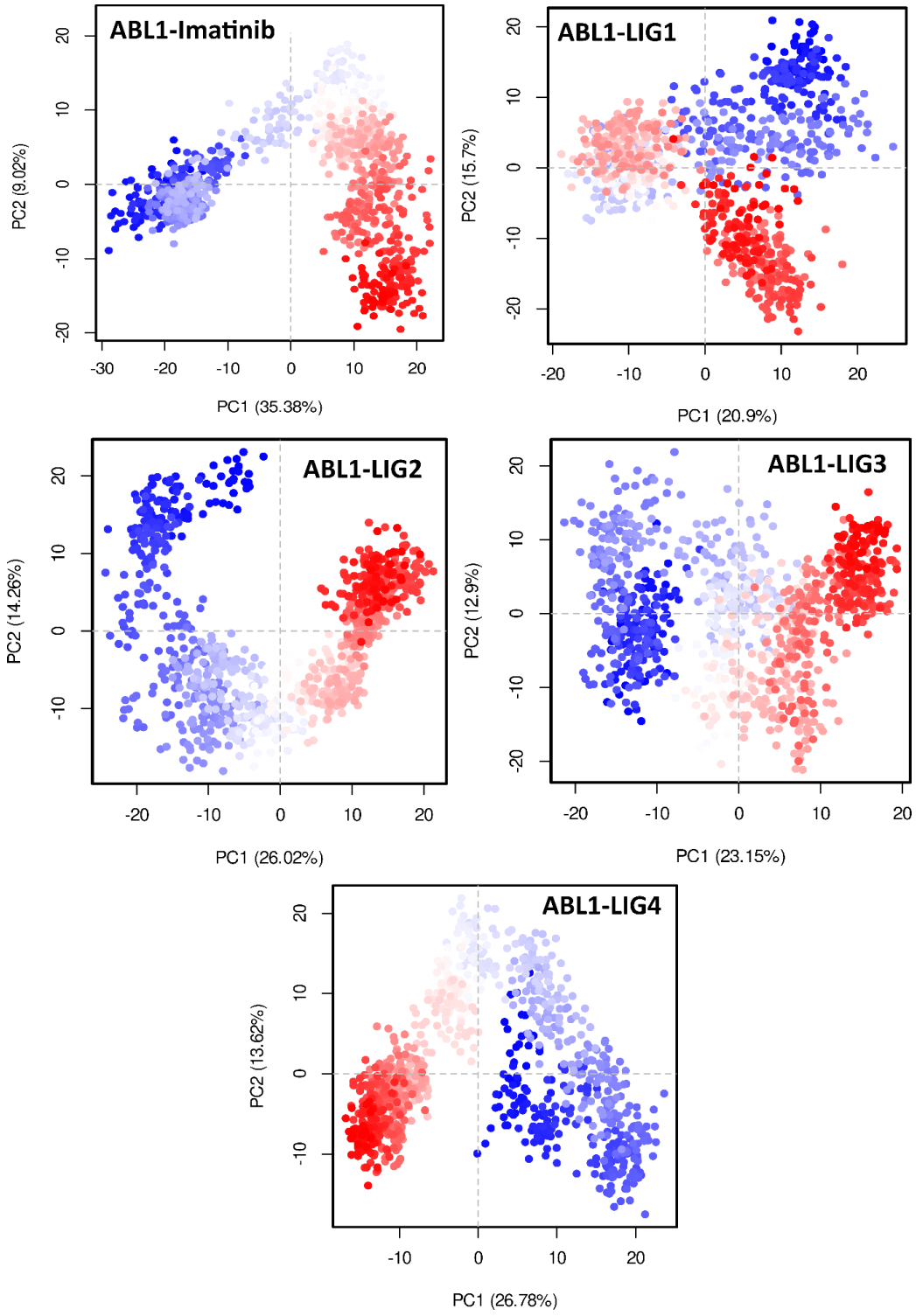

Figure 8: Illustration of PCA plots of LIG1, LIG2, and LIG3, displaying the covariance shared by principal components 1 and 2 (PC1 and PC2), which is responsible for the overall movement of ABL1 atom positions.

Solvent Accessible Surface Area (SASA)

Biomolecules' arrangements and functions are largely determined by their solvent-accessible surface area, or SASA. Amino acid residues on the surface of proteins typically function as active sites or interact with other molecules and ligands, providing information on the components of protein-ligand interactions as well as the solvent-like behaviour (hydrophilic or hydrophobic). The accompanying figure shows the SASA values that were calculated for the protein complexes, which include ABL1-imatinib, ABL1-LIG1, ABL1-LIG2, ABL1-LIG3, and ABL1-LIG4, as shown in **Figure 9**. The average SASA values in these complex systems range from 13000 to 15500, suggesting that certain amino acid residues are largely exposed to the chosen ligand molecules. The 100 ns simulated interaction diagram was used to calculate the solvent-accessible surface area (SASA) of the protein-ligand interaction complexes, where control (ABL1-imitinib) ABL1-LIG1, ABL1-LIG2, ABL-LIG3, ABL1-LIG4, respectively.

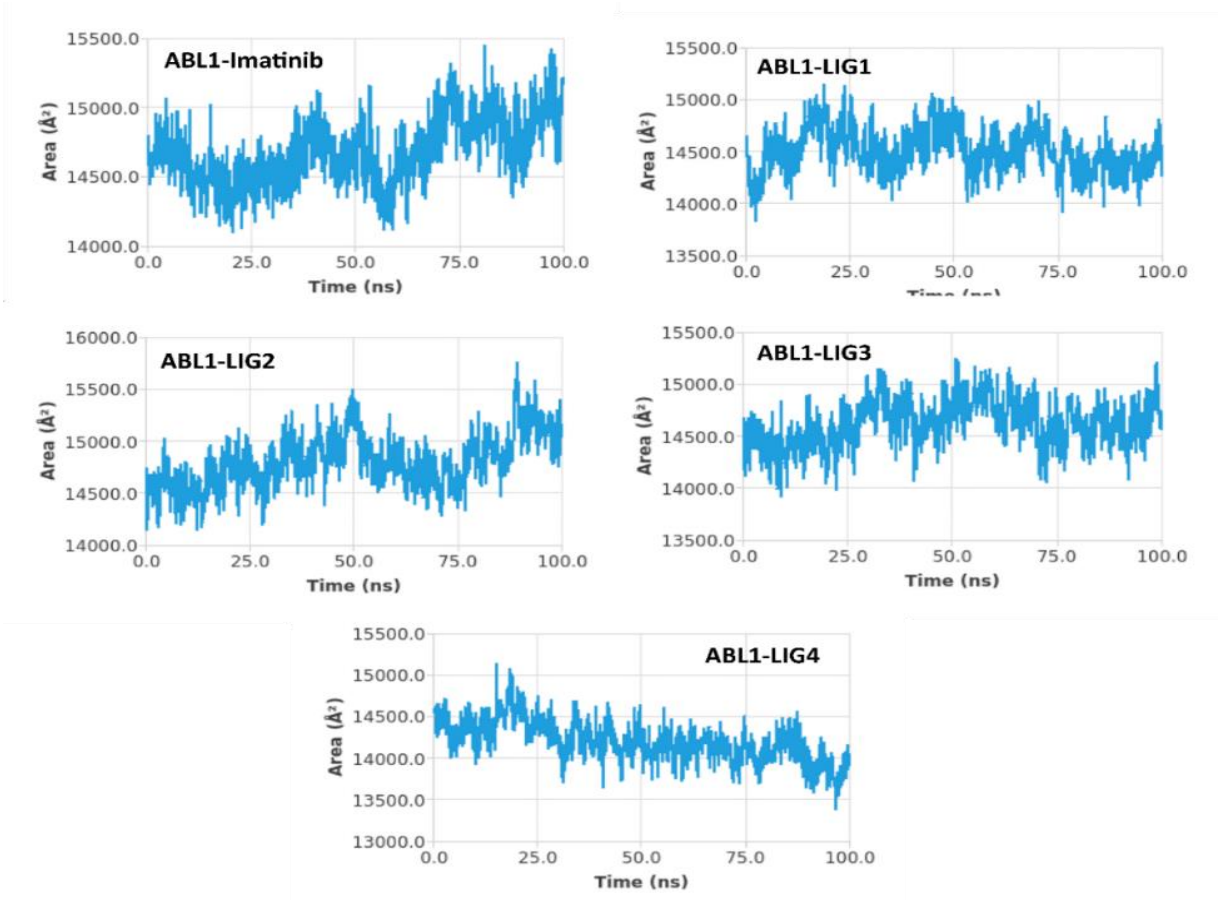

Figure 9: Solvent accessible surface area (SASA) of the ABL1 bounded with selected as a function of time from the MD simulations.

Bioavailability, Drug-Likeness, and ADMET Properties

Pharmacokinetics describes the absorption, distribution, metabolism, and excretion (ADME) of drug molecules following their administration in the body **[35].** Evaluation of these parameters is essential for the successful development and optimisation of drug candidates. In addition, early assessment of toxicity profiles is critical during preclinical and clinical stages to ensure the safety of potential therapeutic agents. In recent years, computer-aided drug design (CADD) approaches have significantly accelerated the drug discovery process by enabling the prediction of pharmacokinetic and toxicological properties at early stages **[36].** ADMET (Absorption, Distribution, Metabolism, Excretion, and Toxicity) profiling provides valuable insights into the physicochemical and drug-likeness properties of candidate molecules, facilitating the identification of compounds with favourable pharmacological profiles.

In silico ADMET analysis was performed for the selected inhibitors (LIG1–LIG4) to evaluate their suitability as potential drug candidates. Key pharmacokinetic parameters, including gastrointestinal (GI) absorption, blood–brain barrier (BBB) permeability, cytochrome P450 (CYP) enzyme interactions, and P-glycoprotein (P-gp) substrate characteristics, were predicted using the SwissADME tool. The results indicate that all selected compounds exhibit high gastrointestinal absorption, suggesting favourable oral bioavailability. Furthermore, the compounds comply with Lipinski's rule of five, indicating acceptable drug-likeness and molecular properties suitable for oral administration. Most of the compounds showed limited BBB permeability, which may reduce the likelihood of central nervous system-related side effects. In terms of metabolic interactions, the selected inhibitors demonstrated minimal inhibition of major CYP450 isoforms, suggesting a lower risk of drug–drug interactions. Additionally, the predicted P-gp substrate profiles indicate that some compounds may be subject to efflux mechanisms, which could influence their bioavailability and distribution.

These compounds showed favorable *computationally predicted* ADMET properties, including absorption, distribution, metabolic stability, and safety profiles. These are preliminary in silico predictions only and require formal experimental validation in cellular and preclinical models.

BOILED-EGG Model for Blood–Brain Barrier (BBB) Permeability and Gastrointestinal (GI) Absorption

The blood–brain barrier (BBB) represents a major challenge in drug development, as it restricts the penetration of most small molecules into the central nervous system (CNS) **[37].** It is estimated that over 98% of small-molecule drugs are unable to cross the BBB, making permeability an important consideration during the early stages of therapeutic design **[38].** In contrast, gastrointestinal (GI) absorption is a key determinant of oral bioavailability and is therefore a critical parameter in the evaluation of drug candidates.

The BOILED-EGG (Brain Or Intestinal Estimated permeation predictive model) is a widely used computational approach for predicting passive human GI absorption and BBB permeability based on physicochemical properties of compounds, particularly lipophilicity (logP) and topological polar surface area (TPSA). This model classifies compounds into distinct regions: the "white" region represents molecules with a high probability of passive GI absorption, while the "yellow" region (yolk) indicates compounds likely to penetrate the BBB.

In addition, the model incorporates the role of P-glycoprotein (P-gp), an ATP-binding cassette (ABC) transporter that actively effluxes xenobiotics and drugs from cells **[39].** P-gp plays a significant role in limiting drug absorption and distribution, contributing to multidrug resistance (MDR) in cancer therapy **[40,41].**

In the present study, the BOILED-EGG analysis revealed that most of the identified inhibitors (LIG1–LIG3) fall within the region associated with high gastrointestinal absorption, indicating favourable oral bioavailability. However, limited BBB permeability was observed for these compounds, which may reduce potential central nervous system side effects. Additionally, the predicted P-gp substrate profile suggests that these compounds may be subjected to efflux mechanisms, which should be considered in further optimisation and experimental validation.

Overall, the BOILED-EGG model supports the drug-likeness and pharmacokinetic suitability of the selected compounds, highlighting their potential as orally bioavailable ABL1 inhibitors for further development.

Table 3: Physiochemical properties and Lipinski rule of five violation of the selected inhibitors.

Compounds	**M/w**	**H. bonds acceptor**	**H. bonds donor**	**Log p**	**Lipinski**	**Num. Rotatable bonds**
Imatinib	494.61 g/mo	5	3	4.04	yes	8
ZINC98605055 (LIG1)	333.43 g/mol	3	3	2.21	yes	6
ZINC98603938 (LIG2)	368.49 g/mol	3	2	3.22	yes	4
ZINC98605017 (LIG3)	334.50 g/mol	5	2	3.75	yes	5
ZINC98604470 (LIG4)	276.40 g/mol	2	1	3.05	yes	3

Table 4: Pharmacokinetic properties of the selected inhibitors.

Compounds	**GI absorption**	**BBB permeant**	**P-gp substrate**	**CYP1A2**	**CYP2C19**	**CYP2C9**	**CYP2D6**	**CYP3A4**	**Lipinski role**
Imatinib	High	No	Yes	Yes	Yes	No	No	No	Yes
ZINC98605055 (LIG1)	High	No	Yes	No	No	No	No	No	Yes
ZINC98603938 (LIG2)	High	No	Yes	No	No	No	No	No	Yes
ZINC98605017 (LIG3)	High	No	Yes	No	No	No	No	No	Yes
ZINC98604470 (LIG4)	High	Yes	Yes	No	No	No	No	No	Yes

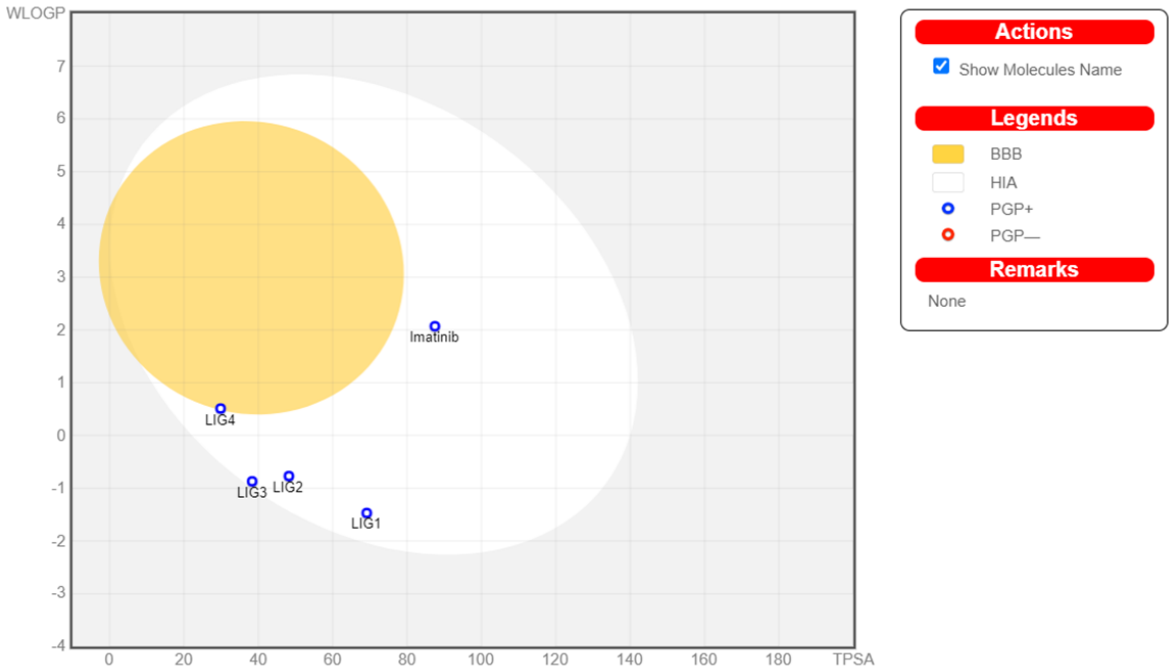

Figure 10: BOILED-EGG model of the selected inhibitors along with the co-crystalline ligand (control) bound in the pocket of the ABL receptor.

Our four lead compounds demonstrated favorable docking scores, stable binding interactions, and promising predicted ADMET properties in silico. These findings support further preclinical investigation to validate inhibitory activity, test against common resistance mutations such as T315I, and assess potential synergy with approved TKIs or immunotherapies. Ongoing clinical trials combining targeted ABL1 inhibition with immunotherapy highlight the importance of developing novel, safe, and effective agents to improve long-term outcomes for children with Ph+ ALL. Acquired resistance via kinase-domain mutations—most notably the T315I gatekeeper mutation—remains a major clinical limitation of current TKIs. Our lead compounds form stable interactions with key conserved residues within the ABL1 active site, suggesting potential to retain binding even in the presence of common resistance variants. However, dedicated structural modeling against mutated ABL1 and functional laboratory testing are essential to confirm activity against resistant leukemia clones in future work.

Study Limitations

This retrospective study is limited by the lack of complete Philadelphia chromosome status and BCR-ABL transcript subtype data for the patient cohort, which prevented formal subgroup

stratification. Consequently, the broad range of observed BCR-ABL expression likely reflects a mixed population of Philadelphia chromosome-positive cases with high oncogenic expression and negative cases with low-level transcript detection. Future prospective studies with confirmed cytogenetic status are recommended to validate these expression patterns further. Despite this limitation, our findings confirm heterogeneous BCR-ABL expression and support the rationale for developing novel ABL1-targeted inhibitors providing promising lead compounds for future experimental validation.

Conclusion

In conclusion, the present study provides an integrated analysis of BCR-ABL expression and the identification of potential ABL1 inhibitors in paediatric acute lymphoblastic leukaemia. Quantitative real-time PCR analysis demonstrated heterogeneous expression of the BCR-ABL fusion oncogene, with substantial inter-patient variability, highlighting its role in leukemogenesis and its potential as a therapeutic target.

Building on these findings, a computational drug discovery approach was employed to identify novel inhibitors targeting the ABL1 kinase domain. Molecular docking and virtual screening identified four lead compounds show more favorable docking scores and stable predicted binding interactions than the reference inhibitor imatinib. These compounds exhibited stable interactions within the active site, which were further supported by molecular dynamics simulations demonstrating favourable structural stability and consistent interaction profiles over time. Additionally, in silico ADMET and pharmacokinetic analyses indicated that the selected compounds possess desirable drug-like properties and acceptable safety profiles.

Overall, this study underscores the importance of integrating experimental gene expression analysis with computational drug discovery approaches to better understand disease mechanisms and identify potential therapeutic candidates. While the identified compounds show promising in silico characteristics, further in vitro and in vivo validation is required to confirm their efficacy and clinical applicability. This integrated strategy may contribute to the development of more effective targeted therapies for BCR-ABL–positive acute lymphoblastic leukaemia.

Availability of data and materials

Data from this study will be made available upon reasonable request.

Author Contribution

Conceptualisation, Shahid Ullah ; methodology, software Shahid Ullah and Carlos Eliel Maya-Ramírez, writing—original draft preparation Muhammad Arif Lodhi, Shahid Ullah, Alex Tonks. All authors have read and agreed to the published version of the manuscript."

Funding Statement

This research received no external funding.

Conflict of interest

The authors declare no conflict of interest.

Acknowledgement: The Authors wish to thank the Higher Education Commission of Pakistan, Department of Hematology, Division of Cancer and Genetics, Cardiff University, School of Medicine, Cardiff, UK, and the Biochemistry Department of Abdul Wali Khan University, Mardan, Pakistan.

Ethics Approval: Approval NO. Dir A&R AWKUM 2020/5118 was received for the current study from Abdul Wali Khan University's Institute Review Board (IRB), located in Mardan, KPK, and Pakistan.

Consent to participate

The institutional review boards or independent ethics committees of all investigational sites approved the protocol, and Informed consent was obtained from all patients' parents involved in the study.

References

1. Rowley, J. D. Chromosome translocations: dangerous liaisons revisited. *Nat. Rev. Cancer* **2001**, *1*(3), 245-250.
2. Leoni, V.; Biondi, A. Tyrosine kinase inhibitors in BCR-ABL positive acute lymphoblastic leukemia. *Haematologica* **2015**, *100*(3), 295.
3. Hui-yu, L.; Guo-Lin, Z.; Ping, Z. The study on BCR/ABL fusion gene in adult acute lymphoblastic leukemia. *Wuhan Univ. J. Nat. Sci.* **2001**, *6*, 742-746.

4. Jain, S.; Abraham, A. BCR-ABL1–like B-acute lymphoblastic leukemia/lymphoma: a comprehensive review. *Arch. Pathol. Lab. Med.* **2020**, *144*(2), 150-155.
5. Roberts, K. G.; Mullighan, C. G. Genomics in acute lymphoblastic leukaemia: insights and treatment implications. *Nat. Rev. Clin. Oncol.* **2015**, *12*(6), 344-357.
6. Bustin, S. A. The MIQE guidelines: minimum information for publication of quantitative real-time PCR experiments. *Clin. Chem.* **2009**, *55*, 461-622.
7. Livak, K. J.; Schmittgen, T. D. Analysis of relative gene expression data using real-time quantitative PCR and the 2− ΔΔCT method. *Methods* **2001**, *25*(4), 402-408.
8. Georgoulia, P. S.; Todde, G.; Bjelic, S.; Friedman, R. The catalytic activity of Abl1 single and compound mutations: Implications for the mechanism of drug resistance mutations in chronic myeloid leukaemia. *Biochim. Biophys. Acta (BBA) - Gen. Subj.* **2019**, *1863*(4), 732-741.
9. Zhong, H. A.; Almahmoud, S. Docking and selectivity studies of covalently bound Janus kinase 3 inhibitors. Int. J. Mol. Sci. 2023, 24 (7), 6023.
10. Moshawih, S.; Goh, H. P.; Kifli, N.; Darwesh, M. A. E.; Ardianto, C.; Goh, K. W.; Ming, L. C. Identification and optimization of TDP1 inhibitors from anthraquinone and chalcone derivatives: consensus scoring virtual screening and molecular simulations. J. Biomol. Struct. Dyn. 2023, 1-25.
11. Vyboishchikov, S. F. Predicting Solvation Free Energies Using Electronegativity-Equalization Atomic Charges and a Dense Neural Network: A Generalized-Born Approach. J. Chem. Theory Comput. 2023, 19 (22), 8340-8350.
12. Ghufran, M.; Ullah, M.; Khan, H. A.; Ghufran, S.; Ayaz, M.; Siddiq, M.; Bungau, S. In-silico lead druggable compounds identification against SARS COVID-19 main protease target from in-house, chembridge and zinc databases by structure-based virtual screening, molecular docking and molecular dynamics simulations. Bioengineering 2023, 10 (1), 100.
13. Ahmad, B.; Saeed, A.; Castrosanto, M. A.; Amir Zia, M.; Farooq, U.; Abbas, Z.; Khan, S. Identification of natural marine compounds as potential inhibitors of CDK2 using molecular docking and molecular dynamics simulation approach. J. Biomol. Struct. Dyn. 2023, 41 (17), 8506-8516.
14. Ahmed, B.; Khan, S.; Nouroz, F.; Farooq, U.; Khalid, S. Exploring multi-target inhibitors using in silico approach targeting cell cycle dysregulator–CDK proteins. J. Biomol. Struct. Dyn. 2022, 40 (19), 8825-8839.
15. Lokhande, K. B.; Doiphode, S.; Vyas, R.; Swamy, K. V. Molecular docking and simulation studies on SARS-CoV-2 Mpro reveals Mitoxantrone, Leucovorin, Birinapant, and Dynasore as potent drugs against COVID-19. J. Biomol. Struct. Dyn. 2021, 39 (18), 7294-7305.
16. Zhang, J.; Zhang, J. LBFGS Quasi-Newtonian Methods for Molecular Modeling Prion AGAAAAGA Amyloid Fibrils. In Molecular Structures and Structural Dynamics of Prion Proteins and Prions: Mechanism Underlying the Resistance to Prion Diseases; 2015; pp 291-307.

17. Quoika, P. K.; Zacharias, M. Liquid–Vapor Coexistence and Spontaneous Evaporation at Atmospheric Pressure of Common Rigid Three-Point Water Models in Molecular Simulations. J. Phys. Chem. B 2024.
18. Ke, Q.; Gong, X.; Liao, S.; Duan, C.; Li, L. Effects of thermostats/barostats on physical properties of liquids by molecular dynamics simulations. J. Mol. Liq. 2022, 365, 120116.
19. Sri Harish, M.; Patra, P. K. Temperature and its control in molecular dynamics simulations. Mol. Simul. 2021, 47 (9), 701-729.
20. Chen, L.; Cruz, A.; Roe, D. R.; Simmonett, A. C.; Wickstrom, L.; Deng, N.; Kurtzman, T. Thermodynamic decomposition of solvation free energies with particle mesh Ewald and long-range Lennard-Jones interactions in Grid Inhomogeneous Solvation Theory. J. Chem. Theory Comput. 2021, 17 (5), 2714-2724.
21. Liang, J.; Tan, P.; Zhao, Y.; Li, L.; Jin, S.; Hong, L.; Xu, Z. Superscalability of the random batch Ewald method. J. Chem. Phys. 2022, 156 (1).
22. Shi, B.; Pang, X.; Li, S.; Wu, H.; Shen, J.; Wang, X.; Jiang, Z. Short hydrogen-bond network confined on COF surfaces enables ultrahigh proton conductivity. Nat. Commun. 2022, 13 (1), 6666.
23. Zhang, D. T.; Baldauf, L.; Roet, S.; Lervik, A.; van Erp, T. S. Highly parallelizable path sampling with minimal rejections using asynchronous replica exchange and infinite swaps. Proc. Natl. Acad. Sci. 2024, 121 (7), e2318731121.
24. Weng, Y. L.; Naik, S. R.; Dingelstad, N.; Lugo, M. R.; Kalyaanamoorthy, S.; Ganesan, A. Molecular dynamics and in silico mutagenesis on the reversible inhibitor-bound SARS-CoV-2 main protease complexes reveal the role of lateral pocket in enhancing the ligand affinity. Sci. Rep. 2021, 11 (1), 7429.
25. Abu-Shady, M.; Inyang, E. P. The fractional Schrodinger equation with the generalized Woods-Saxon potential. arXiv preprint arXiv:2302.03060, 2023.
26. Ahamad, S.; Kanipakam, H.; Birla, S.; Ali, M. S.; Gupta, D. Screening Malaria-box compounds to identify potential inhibitors against SARS-CoV-2 Mpro, using molecular docking and dynamics simulation studies. Eur. J. Pharmacol. 2021, 890, 173664.
27. Pang, M. H.; Liu, X. F.; Tan, X. G.; Wang, Y. Q. A molecular dynamics investigation of drug dissociation from SGLT and its implication in antidiabetic medication development. New J. Chem. 2023, 47 (43), 19933-19942.
28. Singh, E.; Jha, R. K.; Khan, R. J.; Kumar, A.; Jain, M.; Muthukumaran, J.; Singh, A. K. A computational essential dynamics approach to investigate structural influences of ligand binding on Papain like protease from SARS-CoV-2. Comput. Biol. Chem. 2022, 99, 107721.
29. Wu, S. L.; Wang, L. F.; Sun, H. B.; Wang, W.; Yu, Y. X. Probing molecular mechanism of inhibitor bindings to bromodomain-containing protein 4 based on molecular dynamics simulations and principal component analysis. SAR QSAR Environ. Res. 2020, 31 (7), 547-570.
30. Kiriiri, G. K.; Njogu, P. M.; Mwangi, A. N. Exploring different approaches to improve the success of drug discovery and development projects: a review. Future J. Pharm. Sci. 2020, 6, 1-12.

31. Zhuravleva, S. I.; Zadorozhny, A. D.; Shilov, B. V.; Lagunin, A. A. Prediction of Amino Acid Substitutions in ABL1 Protein Leading to Tumor Drug Resistance Based on “Structure-Property” Relationship Classification Models. Life 2023, 13 (9), 1807.
32. Roy, R.; Paul, S. Illustrating the effect of small molecules derived from natural resources on amyloid peptides. J. Phys. Chem. B 2023, 127 (3), 600-615.
33. Choudhuri, S.; Yendluri, M.; Poddar, S.; Li, A.; Mallick, K.; Mallik, S.; Ghosh, B. Recent advancements in computational drug design algorithms through machine learning and optimization. Kinases Phosphatases 2023, 1 (2), 117-140.
34. Olawale, F.; Olofinsan, K.; Iwaloye, O.; Ologuntere, T. E. Adv. Trad. Med. 2021, 1. https://doi.org/10.1007/s13596-021-00598-z.
35. Grant, B. J.; Skjaerven, L.; Yao, X. Q. Protein Sci. 2021, 30, 20. https://doi.org/10.1002/pro.3923.
36. Su, C.; Liu, Y.; Li, R.; Wu, W.; Fawcett, J. P.; Gu, J. Adv. Drug Deliv. Rev. 2019, 143, 97. https://doi.org/10.1016/j.addr.2019.06.008.
37. Ban, F.; Dalal, K.; Li, H.; LeBlanc, E.; Rennie, P. S.; Cherkasov, A. J. Chem. Inf. Model. 2017, 57, 1018. https://doi.org/10.1021/acs.jcim.7b00137.
38. Zhou, X.; Smith, Q. R.; Liu, X. Wiley Interdiscip. Rev. Nanomed. Nanobiotechnol. 2021, 13, e1695.
39. Bernardo-Castro, S.; Sousa, J. A.; Br´as, A.; Cecília, C.; Rodrigues, B.; Almendra, L.; Machado, C.; Santo, G.; Silva, F.; Ferreira, L. Front. Neurol. 2020, 11, 1605. https://doi.org/10.3389/fneur.2020.594672.
40. O’Shea, J. P.; Augustijns, P.; Brandl, M.; Brayden, D. J.; Brouwers, J.; Griffin, B. T.; Holm, R.; Jacobsen, A.-C.; Lennern¨as, H.; Vinarov, Z. Eur. J. Pharm. Sci. 2022, 170, 106098. https://doi.org/10.1016/j.ejps.2021.106098.
41. Chen, Z.; Shi, T.; Zhang, L.; Zhu, P.; Deng, M.; Huang, C.; Hu, T.; Jiang, L.; Li, J. Cancer Lett. 2016, 370, 153. https://doi.org/10.1016/j.canlet.2015.10.010